

Non-linear evolution in $f(R)$ gravity: iterative modelling of the Chameleon mechanism

Sharvari Nadkarni-Ghosh ^{1*} and Tanush Reddy Vaka ^{2†}

¹Department of Space, Planetary and Astronomical Sciences and Engineering (SPASE), I.I.T. Kanpur, Kanpur, U.P. 208016 India.

²School of Physical Sciences, National Institute of Science Education and Research (NISER), Jatni, Khorda, Odisha, 752050 India.

ABSTRACT

We investigate the non-linear evolution of matter perturbations in $f(R)$ models with the Chameleon screening mechanism. The novel feature of our investigation is an iterative solution for the non-linear equation for the scalar field $\chi = \Phi - \Psi$, where Φ and Ψ are the potentials that characterise scalar perturbations of the metric. We demonstrate the scheme on spherical perturbations - smooth, compensated top-hats of varying length scales. We find that the effect of the Chameleon mechanism is seen most prominently on scales where the size of the top-hat is comparable to the Compton scale of the background. There is a density enhancement near the outer edge of the top-hat and the top-hat does not retain its shape. We explain this well-known observation in the context of the spatio-temporal evolution of the Compton scale. Additionally, we find a slight enhancement of the density near the origin, a feature not reported previously in the literature. On scales much smaller or much larger than the background Compton length, including the Chameleon screening has no appreciable effect on the perturbations. In the former, the growth is enhanced as compared to GR and is almost the same as GR in the latter. Finally, we examine the non-linear density velocity divergence (DVDR) relation and find that for evolution affected by Chameleon screening, the DVDR is no longer one-to-one even for a single profile. The relation between density and velocity depends on the location within the perturbation.

Key words: cosmology: theory - large-scale structure of Universe - dark energy

1 INTRODUCTION

The standard Λ CDM model of cosmology faces multiple challenges. On the theoretical front, the origins of dark matter and dark energy are unknown. On the observational front, there are several inconsistencies in the data, most notably the Hubble and σ_8 tensions. Thus, there is a pressing need to investigate theories beyond the standard model. Broadly speaking, there are two approaches to the modifying the standard model. Either the nature of dark energy is modified from the theoretically proposed cosmological constant to some other phenomenological model such as quintessence (Tsujikawa 2013; Tsujikawa & Amendola 2015), or the Einsteinian action is modified, which gives rise to equations that are different from those of the standard GR model (for e.g., Sotiriou & Faraoni (2010); De Felice & Tsujikawa (2010); Clifton et al. (2012); Nojiri et al. (2017)). For some class of models, these two approaches are rendered equivalent by certain mathematical transformations but more generally, they are different (see for e.g., Joyce et al. 2015, 2016; Wetterich 2015). In most modifications, the additional degree of freedom introduced by the modification allows one to recover the background Λ CDM expansion history exactly. Therefore, observations that rely on the background geometry of the Universe, alone, are not enough to distinguish these models from each other or from Λ CDM. Thus, modifications to Λ CDM necessarily need to be constrained by tracking the growth of perturbations. Indeed, many current and upcoming surveys such as SDSS¹, Euclid², DESI³ and the Vera C. Rubin

* E-mail:nsharvari@gmail.com, sharvari@iitk.ac.in (Corresponding Author)

† E-mail:tanushreddy.vaka@niser.ac.in

¹ <https://www.sdss.org>

² <http://sci.esa.int/euclid/>.

³ <https://www.desi.lbl.gov/>

Observatory⁴ all aim to measure the matter distribution at different epochs with the primary aim of constraining cosmological parameters (Alam et al. 2017; Amendola et al. 2018; Alam et al. 2020).

Einstein's gravity has been very well tested on solar system scales. Thus, any viable modified gravity model has to include a screening mechanism through which Einstein's gravity can be recovered in high density, strong gravity regimes such as the solar system, while allowing for deviations on larger cosmological scales and lower density contrasts. In this paper, we focus on one particular class of models, the $f(R)$ models, wherein the Ricci scalar R in the Einstein-Hilbert action is replaced with a general function $f(R)$ and the screening mechanism in these models is referred to as the 'Chameleon Mechanism' (Khoury & Weltman 2004a). In this mechanism, the Compton scale associated with the extra degree of freedom is density-dependent. In high density regions, the Compton scale drops to a very small value and effects of the modification are not felt in most of the domain; GR is recovered. While, this screening mechanism is invoked to ensure consistency with solar system and other local tests of GR, this also has consequences on how structures grow in $f(R)$ gravity scenarios.

Modelling the growth of large scale structure in modified gravity is a more complex task than in standard gravity. In order to appreciate this, it is instructive to understand the difference in the structure of the equations in the two cases. In standard GR, the 'Newtonian' gravitational potential Ψ , which dictates particle dynamics and appears in the Euler equation is the same as the potential Φ which appears in the Poisson equation. The Laplacian in the Poisson equation is a linear operator acting on the field Φ and hence the potential can be easily solved using analytic forms or Fourier Transforms in case of Gaussian periodic initial conditions. In contrast, in most MG models, the equality between Φ and Ψ is violated and an extra spatial equation is necessary to evolve the two potentials simultaneously. If one includes the Chameleon mechanism, then one of these equations is a non-linear equation in the field and cannot be solved by simple Fourier transforms. Instead, one has to invoke more sophisticated solvers in the spatial domain. These numerical complexities do not arise in linear theory, where the main consequence of the additional degree of freedom is that the growth rate becomes scale dependent (e.g., Brax et al. (2006); Song et al. (2007); Bean et al. (2007); Pogosian & Silvestri (2008); Song et al. (2007)). It also does not arise in non-linear modelling, if the Chameleon mechanism is ignored.

In pioneering work, Oyaizu (2008) laid down the basic numerical scheme to incorporate the effect of the Chameleon mechanism in $f(R)$ theories. The method uses multi-grid method for solving the equations, which involves using a hierarchy of grids with successively decreasing but pre-determined resolution. This was used by collaborators to study the non-linear matter power spectrum and the distribution of haloes (Oyaizu et al. 2008; Schmidt et al. 2009). Zhao et al. 2011 improved upon this by treating the high density regions with a mesh with self-adaptive resolution. This approach was used to incorporate modified gravity models into the hydrodynamic code GADGET (Puchwein et al. 2013). Similar numerical techniques were combined with the Zeldovich approximation and its extensions with the aim of increasing computational efficiency (Vraštil & Habib 2020) There have also been efforts to model non-linear growth in $f(R)$ models using Eulerian Perturbation Theory (e.g., Koyama et al. 2009), Lagrangian Perturbation Theory (e.g., Aviles & Cervantes-Cota 2017) and the COLA approach (Tassev et al. 2013; Valogiannis & Bean 2017; Winther et al. 2017) which combines LPT evolution on large scales with N-body evolution on small scales. More recent investigations have compared numerical and approximate schemes across different types of MG models (Winther et al. 2015; Llinares 2018; Bose et al. 2024).

One of the major drawbacks of N-body simulations is that they are slow. Furthermore, they employ a discrete representation of particles to represent continuous fields. The problem is exacerbated as the starting redshift increases and more particles are necessary to maintain accuracy. The use of additional non-FFT based methods to solve the extra scalar field further slows down the computation. Often, in standard gravity, semi-analytic methods such as the Press-Schechter formalism prove to be useful estimates to predict the mass function Press & Schechter (1974); Sheth et al. (2001). These models usually employ geometric methods such as spherical or triaxial collapse as a proxy for the non-linear regime. Such geometric methods can also provide useful insights into the non-linear density-velocity divergence relation (DVDR) (Bilicki & Chodorowski 2008; Nadkarni-Ghosh 2013; Nadkarni-Ghosh & Singhal 2016), can be useful to estimate the one-point PDF in non-standard models (Cataneo et al. 2021; Mandal & Nadkarni-Ghosh 2020) and can also model the evolution of halo axes ratios. However, even implementing the spherical collapse (SC) model in modified gravity is not as simple as in standard GR. (Lee et al. 2005; Nadkarni-Ghosh & Arya 2018). In this paper, we build upon previous investigation of Nadkarni-Ghosh & Chowdhury (2022); hereafter NC22, which considered spherical top-hat collapse in $f(R)$ models, but in the absence of the chameleon mechanism. One of the main aims of that paper was to understand the joint evolution of the density and velocity fields in $f(R)$ gravity and compare it to the evolution in standard GR. In standard gravity, the density and velocity divergence are proportional; the proportionality constant is the growth rate, which is a sensitive probe of the underlying cosmology. The linear relation is a consequence of the continuity equation coupled with the linear theory solution which ignores the decaying mode. The density-velocity dynamics has been of interest since the early 1990s Bernardeau (1992); Chodorowski & Lokas (1997); Chodorowski

⁴ <https://www.lsst.org>

et al. (1998); Bernardeau et al. (1999) and indeed many upcoming surveys aim to constrain the growth factor or to test the continuity equation Zheng et al. (2025).

In NC22, a multi-step hybrid Lagrangian-Eulerian scheme was employed to solve for the spherical collapse equations in $f(R)$ gravity. At each step, the Euler and continuity equations were solved in the Lagrangian frame by tracking shell positions. The algebraic equations for the two gravitational potentials Φ and Ψ were re-cast in terms of the variables $\Phi_+ = (\Phi + \Psi)/2$ and $\chi = \Phi - \Psi$ as defined by Pogosian & Silvestri (2008). While Φ_+ satisfies Poisson's equation, χ satisfies a non-linear equation (χ is proportional to the scalar field when mapped to quintessence models). However, if the Chameleon mechanism is ignored then the differential operator χ is linear and analytic solutions are possible. In this paper, we include the Chameleon mechanism by solving the non-linear equation for χ iteratively, albeit exploiting the analytic solution at each iteration. The iterative algorithm proposed is demonstrated on the spherical collapse model, but is a general framework that can be extended to 3D random initial conditions to be solved using Fourier transforms.

Investigations of the spherical top-hat collapse in $f(R)$ models are not new. The seminal papers by Khouri and Weltmann (Khouri & Weltman 2004b,a) illustrate the chameleon mechanism using static, spherically symmetric perturbations. Brax et al. (2010) elaborated on this work and generalized it to include cosmologically evolving spherical perturbations with the aim of computing the critical (linear) density of collapse, δ_c , which is a key ingredient in the Press-Schechter formalism of predicting the halo mass function. Li and collaborators extended this to include effects of the environment, both in Eulerian and Lagrangian space, considered the effect of the nature of the random walk and compared the results with N-body simulations (Li & Efstathiou 2012; Li & Lam 2012; Lam & Li 2012; Lombriser, Li, Koyama, & Zhao 2013). Most investigations with the spherical top-hat culminate in the calculation of δ_c and there have been other investigations with the same aim. Borisov et al. (2012) considered top-hat initial distributions and showed that a top-hat does not retain its top-hat shape in the presence of the chameleon screening. Instead, there is an enhancement of density near the edge of the top-hat potentially leading to shell-crossing. They considered smoothed top-hats to compute δ_c , whose value in turn depended on the smoothing strength i.e. on the specific shape of the profile. In order to give a non-ambiguous estimate of δ_c , Kopp et al. (2013) considered initial profiles which corresponded to average density profiles calculated using the BBKS peaks theory (Bardeen et al. 1986) since they are the most relevant from an observational standpoint. Herrera et al. (2017) also computed δ_c with different ways to approach the epoch of collapse pointing out the role of different numerical definitions of infinite density. Lombriser (2016) provided a parametrized spherical collapse model as a generalization of the linear, parametrized post-Friedmannian formalism to characterise the different effects of the modifications to gravity. Lopes et al. (2018a,b) have investigated the spherical collapse model to compute the virial mass and turn-around radius in $f(R)$ models. In terms of techniques, the approach followed in NC22 and in this paper is similar in spirit to that of Kopp et al. (2013) and Borisov et al. (2012). They solve the coupled continuity, Euler, Poisson and scalar field equations, the former in the Eulerian frame and the latter in the Lagrangian frame. Both use a relaxation method to solve the non-linear two-point boundary value ODE for the scalar field potential exactly. In contrast, we solve for the non-linear equation approximately, relying upon analytic solutions. Our method is approximate, but simpler to implement numerically. Furthermore, none of the earlier investigations of SC have explicitly presented the spatio-temporal evolution of the Compton scale, a key feature of the Chameleon mechanism.

The paper is organised as follows. §2 defines the background $f(R)$ model used in this paper and its associated Compton wavelength. §3 sets up the equations governing non-linear growth of perturbations. §4 explains the method used to solve this system §5 presents the results for the spatio-temporal evolution of the Compton scale, the density and velocity fields. §6 concludes with a discussion and future outlook.

2 THE $f(R)$ MODEL AND THE COMPTON WAVELENGTH

2.1 The Hu-Sawicki model

We consider a cold dark matter fluid evolving in an expanding Universe governed by an $f(R)$ model of gravity with an action of the form

$$S = \frac{1}{2\kappa^2} \int d^4x \sqrt{-g} \{R + f(R)\} + S_m, \quad (1)$$

where $\kappa^2 = 8\pi G$ and S_m is a minimally coupled matter action. Here f is a function of the Ricci curvature scalar R defined as

$$R = (R_{\mu\nu})g^{\mu\nu} \quad (2)$$

$$= \left(\partial_\alpha \Gamma_{\mu\nu}^\alpha - \partial_\mu \Gamma_{\alpha\nu}^\alpha + \Gamma_{\mu\nu}^\beta \Gamma_{\beta\alpha}^\alpha - \Gamma_{\alpha\nu}^\beta \Gamma_{\beta\mu}^\alpha \right) g^{\mu\nu}, \quad (3)$$

where $g_{\mu\nu}$ is the metric and $\Gamma_{\alpha\nu}^\alpha = g^{\alpha\beta} \partial_\nu g_{\alpha\beta}$. In the absence of perturbations, the spatially flat FRW background metric $g_{\alpha\beta}$ is given by

$$ds^2 = -c^2 dt^2 + a(t)^2 (dx^2 + dy^2 + dz^2). \quad (4)$$

and the Ricci scalar for the background, denoted as R_b reduces to

$$R_b \equiv R_b(a) = \frac{12H^2 + 6HH'}{c^2}, \quad (5)$$

where $H = \frac{\dot{a}}{a}$ is the Hubble parameter. Here \cdot and $'$ denote derivative w.r.t. time and $\ln a$ respectively. For a pressure-less (cold) dark matter fluid considered here, the Friedmann equation becomes,

$$H^2 - f_R(HH' + H^2) + \frac{1}{6}f + H^2f_{RR}R' = \frac{\kappa^2\bar{\rho}}{3}, \quad (6)$$

where $\bar{\rho}$ is the homogeneous background density of dark matter, $f_R = df/dR$ and $f_{RR} = d^2f/dR^2$. In standard GR, the Friedmann equation is a second order equation for the scale factor $a(t)$, whereas in the $f(R)$ model, the Friedmann equation becomes fourth order in time. This feature allows for different types of solutions to this equation. One approach is to assert that the background evolution for $H(a)$ is identical to that given by the Λ CDM model, recast the derivatives of f with respect to R in terms of derivatives w.r.t. time and solve the resulting second order equation for f subject to appropriate initial conditions. This is called the designer approach (Song et al. 2007; Pogosian & Silvestri 2008). The other approach is to assume a functional dependence of f on R and choose parameters such that Λ CDM expansion history is recovered in appropriate limits. In this paper, we adopt the latter approach and focus on a particular form of $f(R)$ given by Hu & Sawicki (2007):

$$f(R) = -m^2 \frac{c_1(R/m^2)^n}{c_2(R/m^2)^n + 1}, \quad (7)$$

where $m^2 = H_0^2\Omega_{m0}$ and c_1, c_2 and n are parameters of the model. For a flat Λ CDM expansion history,

$$H_{\Lambda\text{CDM}}^2(a) = H_0^2 \left(\frac{\Omega_{m,0}}{a^3} + \Omega_{\Lambda,0} \right) \quad (8)$$

$$\text{and } R_{\Lambda\text{CDM}}(a) = 3H_0^2 \left(\frac{\Omega_{m,0}}{a^3} + 4\Omega_{\Lambda,0} \right). \quad (9)$$

Demanding that at early epochs, i.e., when $R \rightarrow \infty$, the dynamics should reduce to Λ CDM, gives

$$\frac{c_1}{c_2} \approx 6 \frac{\Omega_{\Lambda,0}}{\Omega_{m,0}}. \quad (10)$$

The parameters n and c_1/c_2 are related to the derivative f_{R0} through

$$f_{R0} \approx -n \frac{c_1}{c_2^2} \left(\frac{12}{\Omega_{m,0}} - 9 \right)^{-n-1}. \quad (11)$$

Thus, given the cosmological parameters, choosing n and f_{R0} completely specifies the model.

In this work, we choose the parameters (same as NC22): $\Omega_{m,0} = 0.32$, $\Omega_{\Lambda,0} = 0.68$, $f_{R,0} = -10^{-6}$, $n = 1$. Certain features of the background evolution are worth noting. Substituting eq. (7) in eq. (6) gives a second order equation for $H(t)$, whose solution, will not be exactly the same as eq. (8). How closely it follows the Λ CDM evolution is determined by n and f_{R0} . The evolution of the effective equation of state w predicted by eqs. (7) and (6) is highly oscillatory making the background evolution very stiff for early starting epochs. This oscillatory behaviour was pointed out in Hu & Sawicki (2007), but its implications on the deviations from Λ CDM were not investigated.

In NC22, we investigated this behaviour and found that the degree of stiffness is connected to the starting epoch of evolution. If the evolution is started at an earlier epoch, then the system more closely follows Λ CDM near the present epoch, but the system is numerically stiff. Starting the evolution later mitigates the stiffness, at the cost of a larger deviation from Λ CDM near the present epoch (see fig. 1 of NC22). This numerical stiffness also present in the perturbation equations. Thus, there is a trade-off between the computational cost arising from the stiffness vs. the error due to deviation from Λ CDM. To address this issue, we track the perturbations using standard GR until an epoch a_{trans} after which we transition to $f(R)$ gravity. To make an informed choice for a_{trans} , we performed an eigenvalue analysis of the background system of equations and chose a_{trans} to be the epoch where the imaginary eigenvalues (responsible for the oscillations) significantly reduced in magnitude (fig. 2 of NC22). We adopt the same approach in this paper.

2.2 The Compton wavelength

The extra degree of freedom associated with the modification, gives rise to an additional force whose range is given by the Compton wavelength. This is expressed as (Hu & Sawicki 2007)

$$\lambda_C = 2\pi \left[\frac{1}{3} \left(\frac{1+f_R}{f_{RR}} - R \right) \right]^{-1} \approx 2\pi\sqrt{3f_{RR}}. \quad (12)$$

We have used the fact that $f_R \ll 1$ and $f_{RR}^{-1} \gg R$ throughout the evolution. The comoving Compton wavelength x_C and the reduced comoving Compton wavelength \bar{x}_C are defined as

$$x_C = \frac{\lambda_C}{a} \quad \text{and} \quad \bar{x}_C = \frac{x_C}{2\pi} \approx \frac{c\sqrt{3f_{RR}}}{a}. \quad (13)$$

Thus, the Compton scale depends on the value of R , the Ricci scalar. In the presence of Chameleon screening, \bar{x}_C changes according to the change in R governed by the change in the matter density. We define the background value of the Compton scale as

$$\bar{x}_{C,b} \approx \left. \frac{c\sqrt{3f_{RR}}}{a} \right|_{R=R_{\Lambda CDM}}, \quad (14)$$

where $R_{\Lambda CDM}$ is given by eq. (9).

3 EQUATIONS GOVERNING PERTURBATIONS.

Here we consider only scalar perturbations of the metric evolving in the background cosmology described above. The perturbations are only in the matter sector with the density contrast given by $\delta = \rho/\bar{\rho} - 1$, where ρ is the density of the perturbations and $\bar{\rho}$ is the background density. $\mathbf{x} = \{x_1, x_2, x_3\}$ denotes the comoving coordinate and $\mathbf{v} = a\dot{\mathbf{x}}$ is the peculiar velocity. The equations presented here and the method in the next section apply to general 3D perturbations. We will restrict to spherical symmetry in §4.3. In the conformal Newtonian Gauge the metric has the form

$$ds^2 = -c^2 \left(1 + \frac{2\Psi}{c^2}\right) dt^2 + a^2 \left(1 - \frac{2\Phi}{c^2}\right) (dx_1^2 + dx_2^2 + dx_3^2) \quad (15)$$

Here Ψ corresponds to the Newtonian potential, which dictates particle motions and Φ is the ‘curvature’ fluctuation. In standard gravity these two fluctuations are the same, but in $f(R)$ models their difference is related to the perturbation in f_R as

$$\Phi - \Psi = c^2 \delta f_R. \quad (16)$$

In standard gravity with Λ CDM, on sub-horizon scales, the Newtonian equations of hydrodynamics corresponding to a compressible, pressure-less, inviscid flow v.i.z., the Euler and the continuity equation coupled with Poisson’s equation describe the evolution of perturbations fairly well. These equations are effectively obtained from the sub-horizon limit of Einstein’s equations ($ck \ll aH$) and the equation governing the conservation of the stress-energy tensor. In modified gravity models, in addition to the sub-horizon approximation, we separately impose the Quasi-static approximation, wherein the potentials Φ and Ψ vary on longer time scales as compared to the expansion time scale H^{-1} ⁵. In this limit, the Einstein equations are (Oyaizu 2008; Schmidt et al. 2009; Borisov et al. 2012)

$$\nabla_x^2 \delta f_R = \frac{a^2 \delta R}{3c^2} - \frac{H^2 a^2 \Omega_m \delta}{c^2} \quad (17)$$

$$\nabla_x^2 \Psi = 2H^2 a^2 \Omega_m \delta - \frac{a^2 \delta R}{6}, \quad (18)$$

where δR is the perturbation to the Ricci scalar R . In a spatially varying density perturbation, R will be a function of \mathbf{x} . From the definition of f_{RR} , we have

$$\delta f_R = f_{RR} \delta R \quad (19)$$

$$\text{or } \delta R = f_{RR}^{-1} \delta f_R = \frac{\Phi - \Psi}{f_{RR} c^2}. \quad (20)$$

We note that this is an exact expression for δR and $f_{RR} \equiv f_{RR}(R)$ is spatially varying since $R \equiv R(\mathbf{x})$. Following (Pogosian & Silvestri 2008) we define the variables

$$\chi = \Phi - \Psi \quad (21)$$

$$\Phi_+ = \frac{\Phi + \Psi}{2}. \quad (22)$$

⁵ In standard Λ CDM gravity, it can be shown that imposing the sub-horizon approximation, automatically imposes the quasi-static approximation. This is not true in other non-standard dark energy models and the two approximations have to be invoked separately.

Substituting eqs. (16), (20), (21) and (22) in eqs. (17) and (18) and combining with the conservation of the stress-energy tensor (Continuity, Euler) gives

$$\frac{\partial \delta}{\partial t} + \left(\frac{\mathbf{v}}{a} \cdot \nabla_x \right) \delta = -\frac{(1+\delta)}{a} (\nabla_x \cdot \mathbf{v}) \quad (23)$$

$$\frac{\partial \mathbf{v}}{\partial t} + \left(\frac{\mathbf{v}}{a} \cdot \nabla_x \right) \mathbf{v} + H \mathbf{v} = -\frac{1}{a} \nabla_x \Psi \quad (24)$$

$$\nabla_x^2 \Phi_+ = \frac{3}{2} H^2 a^2 \Omega_m \delta \quad (25)$$

$$\nabla_x^2 \chi - \frac{a^2}{3c^2 f_{RR}(\mathbf{x}, a)} \chi = -H^2 a^2 \Omega_m \delta. \quad (26)$$

Substituting from eq. (13), we can re-write the last equation as

$$\nabla_x^2 \chi - \frac{1}{\bar{x}_C^2(\mathbf{x}, a)} \chi = -H^2 a^2 \Omega_m \delta. \quad (27)$$

These equations are to be solved for the coupled variables δ , \mathbf{v} , Φ_+ and χ given initial spatial profiles for the δ and \mathbf{v} . The boundary conditions will depend on the geometry at hand (3D or spherical).

The dependence of f_{RR} or \bar{x}_C on the position is indicated explicitly. It is possible to approximate eq. (20) as

$$\delta f_R \approx f_{RR}|_{R=R_b} \delta R + \mathcal{O}(\delta R^2) \quad (28)$$

and consequently drop the position dependence of the Compton scale in eq. (27). This is equivalent to ignoring the Chameleon mechanism as was done in NC22. In general, as the density perturbation grows, R changes as a function of both time as space and consequently so does f_{RR} and the related Compton scale. In this work, we track the change in R and evaluate f_{RR} at the appropriate R . Given the form of the metric in eq. (15), the expression for R is

$$R = \frac{6 [H' H + 2H^2]}{V_\Psi} + \frac{c^2 [V_\Psi (2V_\Psi \Phi'' - V_\Phi \Psi'') + V_\Phi (\Psi')^2]}{a^2 V_\Phi^2 V_\Psi^2} + \frac{c^2 [V_\Phi \Psi' \Phi' + 3V_\Psi^2 (\Phi')^2]}{a^2 V_\Phi^3 V_\Psi}, \quad (29)$$

where $V_\Psi = c^2 + 2\Psi$ and $V_\Phi = c^2 - 2\Phi$. Note that in the absence of perturbations, it reduces to eq. (5).

4 METHOD OF SOLUTION

4.1 Algorithm

We use a hybrid Eulerian-Lagrangian scheme to solve this system of equations. The algorithm to solve this system is similar to that discussed in NC22, except a modification for the solution of χ . We briefly describe the basic method here. The system is evolved using standard GR equations until $a = a_{trans}$ after which $f(R)$ gravity takes over. The interval of interest from a_{trans} to a_{final} is divided into N_t intervals. Let a_n and a_{n+1} denote the starting and stopping epochs of the n -th interval. The evolution between each time-step consists of two operations.

(i) Step I (Solve the spatial equations for the potentials): The spatial equations eq. (25) and (26) are solved for the fields Φ_+ and χ and these fields are assumed to stay constant over the time interval (quasi-static). Thus, at the n -th step we have to solve,

$$\nabla_x^2 \Phi_+ = \frac{3}{2} H^2 a^2 \Omega_m \delta(\mathbf{x}, a_n) \quad (30)$$

$$\nabla_x^2 \chi - \frac{a^2}{3c^2 f_{RR}(\mathbf{x}, a_n)} \chi = -H^2 a^2 \Omega_m \delta(\mathbf{x}, a_n). \quad (31)$$

$\delta(\mathbf{x}, a_n)$ is known at the start of the step. In a general 3D system, the solution for Φ_+ can be obtained using FFTs. If the Chameleon mechanism is ignored, then f_{RR} is not a function of space and the solution for χ can also be obtained directly using FFTs. When the Chameleon mechanism is accounted for, the solution is given by the iterative procedure outlined in §4.2, where each step of the iteration is solved using FFTs. These are solved in the Eulerian frame.

(ii) Step II (Solve the evolution equations for density and velocity): In 3D, the temporal equations for δ and \mathbf{v} can in principle be solved in any frame - Eulerian or Lagrangian using perturbative techniques. They can also be solved using N-body codes. In spherical symmetry, we solve for shell positions which is a Lagrangian approach and will be explicitly laid out in §4.3.

4.2 Iterative solution for the χ field

In the presence of perturbations, the Ricci scalar becomes $R = R_b + \delta R$, where $R_b \equiv R_b(a)$ is the Ricci scalar of the background and δR is the modification due to the perturbation. In principle, δR and hence $f_{RR}|_{R+\delta R}$, depends on χ which makes eq. (31) an implicit non-linear equation. However, we will assume that the dominant contribution to δR is from the estimate of χ in the absence of Chameleon. We then systematically calculate corrections to χ using this value of δR . We assume the ansatz

$$\chi = \sum_{n=1}^{\infty} \epsilon^n \chi^{(n)}, \quad (32)$$

where ϵ is a book-keeping parameter, whose magnitude is of the order of $\delta(\mathbf{x}, a_n)$ or δR . Expanding f_{RR} around $R = R_b$ gives,

$$f_{RR}(R) = f_{RR}|_{R_b} + \sum_{n=1}^{\infty} \frac{df^{n+2}}{dR^{n+2}} \Big|_{R_b} \frac{(\epsilon \delta R)^n}{n!} \quad (33)$$

$$= f_{RR}|_{R_b} \left(1 + \sum_{n=1}^{\infty} F_n (\delta R)^n \epsilon^n \right), \quad (34)$$

where F_n is defined as

$$F_n = \frac{1}{n! f_{RR}|_{R_b}} \frac{df^{n+2}}{dR^{n+2}} \Big|_{R_b}. \quad (35)$$

Substitute in l.h.s. of eq. (26), and identify $\frac{a^2}{3c^2 f_{RR}|_{R_b}} = \frac{1}{\bar{x}_{C,b}^2}$, the Compton wavelength for the background. Substituting eqs. (32) and (34) in eq. (31) gives,

$$\nabla_x^2 \left(\sum_{n=1}^{\infty} \epsilon^n \chi^{(n)} \right) - \frac{1}{\bar{x}_c^2} \left(\sum_{n=1}^{\infty} \epsilon^n \chi^{(n)} \right) \cdot \left(1 + \sum_{n=1}^{\infty} F_n (\delta R)^n \epsilon^n \right)^{-1} = -H^2 a^2 \Omega_m \delta(\mathbf{x}, a_n). \quad (36)$$

Equating order-wise, gives at first order

$$\nabla_x^2 \chi^{(1)} - \frac{1}{\bar{x}_{C,b}^2} \chi^{(1)} = H^2 a^2 \Omega_m \delta(\mathbf{x}, a_n). \quad (37)$$

Along with $\chi^{(1)}$, solve eq. (30) for Φ_+ . Next, compute δR as

$$\delta R = R - R_b(a_n), \quad (38)$$

where R is given by eq. (29). The Φ and Ψ appearing in eq. (29) are evaluated from Φ_+ and $\chi = \chi^{(1)}$. This δR is fixed for the remaining iterations for χ . Equating the higher order ϵ terms, gives equations for the correction terms as:

$$\nabla_x^2 \chi^{(2)} - \frac{1}{\bar{x}_c^2} \chi^{(2)} = \frac{1}{\bar{x}_c^2} F_1(\delta R) \chi^{(1)} \quad (39)$$

$$\nabla_x^2 \chi^{(3)} - \frac{1}{\bar{x}_c^2} \chi^{(3)} = \frac{1}{\bar{x}_c^2} \left\{ (F_1^2 - F_2) (\delta R)^2 \chi^{(1)} - F_1(\delta R) \chi^{(2)} \right\} \quad (40)$$

$$\nabla_x^3 \chi^{(4)} - \frac{1}{\bar{x}_c^2} \chi^{(4)} = -\frac{1}{\bar{x}_c^2} \left\{ (F_1^3 - 2F_1 F_2 + F_3) (\delta R)^3 \chi^{(1)} + (F_2 - F_1^2) (\delta R)^2 \chi^{(2)} + F_1(\delta R) \chi^{(3)} \right\} \quad (41)$$

In this paper we stop at a fourth order expansion in ϵ . The higher order source terms are generated from the knowledge of lower order solutions. It is easy to generate these expansions using a symbolic software like Mathematica.

The above framework is general and can be solved subject to initial conditions depending upon the geometry. Typically for a 3D system with random Gaussian initial conditions in a periodic box, solutions for $\chi^{(1,2,3,4)}$ can be solved using FFTs. In this paper, we demonstrate the method in a spherically symmetric system. The boundary conditions take the form.

$$\Phi_+(x \rightarrow \infty) = 0, \quad \frac{\partial \Phi_+}{\partial x} \Big|_{x=0} = 0 \quad (42)$$

$$\chi(x \rightarrow \infty) = 0, \quad \frac{\partial \chi}{\partial x} \Big|_{x=0} = 0. \quad (43)$$

The boundary conditions on χ can be re-written for each approximation to χ as

$$\chi^{(n)}(x \rightarrow \infty) = 0, \quad \frac{\partial \chi^{(n)}}{\partial x} \Big|_{x=0} = 0 \quad \text{for } n = 1, 2, 3, 4. \quad (44)$$

At each order we use the analytic solution for χ presented in NC22. Appendix §A1 presents the convergence test of this approach implemented on a spherically symmetric initial profile δ .

4.3 Spherically Symmetric Perturbations

We consider a radially varying density and velocity perturbation in spherical symmetry. We solve the coupled Euler and continuity equations in the Lagrangian frame, which physically corresponds to tracking positions of concentric spherical shells. Let origin be the centre of the sphere. The Lagrangian coordinate of any shell is taken to be its initial comoving coordinate \mathbf{q} at the start of the step. The Eulerian coordinate at any later epoch is given by

$$x \equiv x(q, a) = A(q, a)q, \quad (45)$$

where $A(q, a)$ can be thought of as the scale factor of the shell at q . The density at the end of the step at $\delta(q, a_{n+1})$ is related to the density at the start of the step $\delta(q, a_n)$ as

$$1 + \delta(q, a_{n+1}) = (1 + \delta(q, a_n)) \frac{q^2 dq}{x^2 dx} = \frac{(1 + \delta(q, a_n))}{A^3 \left| 1 + \frac{q}{A} \frac{dA}{dq} \right|}. \quad (46)$$

It can be easily checked that the density given by the above expression satisfies the continuity equation given by eq. (23). The spherically averaged density is defined as

$$\Delta(x) = \frac{3}{x^3} \int_0^x \delta(x, a) x^2 dx. \quad (47)$$

It satisfies the condition

$$1 + \Delta(q, a_{n+1}) = \frac{(1 + \Delta(q, a_n)) A_{init}^3}{A^3}. \quad (48)$$

The peculiar velocity is given by

$$v(a, q) = a \dot{A} q = a A'(q, a) H(a) q \quad (49)$$

where ‘dot’ denotes the total derivative w.r.t. time t and ‘prime’ denotes derivatives w.r.t. $\ln a$. With these definitions, the Euler equation eq. (24) in Lagrangian variables becomes

$$A'' + \left(2 - \frac{3}{2} \Omega_m(a) \right) A' = -\frac{1}{q} \nabla_q \tilde{\Psi}(q, a), \quad (50)$$

where $\tilde{\Psi} = \Psi/H^2$. It is important to note that the Lagrangian coordinate will change at the start of each step, whereas, by definition $A = 1$ for all shells at the start of the every step. The initial peculiar velocity at the start of the step $v(q, a_n)$ sets the initial conditions for A' at the start of each step. Imposing spherical symmetry, eqs. (30) and (31) for Φ_+ and χ take the form

$$\frac{\partial^2 \tilde{\Phi}_+}{\partial x^2} + \frac{2}{x} \frac{\partial \tilde{\Phi}_+}{\partial x} = \frac{3}{2} a^2 \Omega_m(a) \delta(x, a_n). \quad (51)$$

$$\frac{\partial^2 \tilde{\chi}}{\partial x^2} + \frac{2}{x} \frac{\partial \tilde{\chi}}{\partial x} - \frac{1}{\tilde{x}_C^2} \tilde{\chi} = -a^2 \Omega_m(a) \delta(x, a_n), \quad (52)$$

where $\tilde{\Phi} = \Phi/H^2$, $\tilde{\chi} = \chi/H^2$.

Thus, at each time-step, given the initial density and velocity, we first solve eqs. (51) and eq. (52) for $\tilde{\Phi}_+$ and $\tilde{\chi}$, compute $\tilde{\Psi}$ and then evolve eq. (50) to get the final density and velocity. At each step, the Lagrangian variable is re-defined. The detailed algorithm is given in section 4.5 of NC22.

We consider smooth, compensated top-hat profiles characterized by a length scale x_{top} . The dynamics of the perturbations is governed by a parameter Q defined as the ratio of the top-hat scale to the comoving Compton scale

$$Q = \frac{\tilde{x}_C}{x_{top}}. \quad (53)$$

It should be noted that in presence of Chameleon screening, Q is a time and space dependent quantity. Based on Q , we define three regimes of the dynamics:

(i) The strong-field regime ($Q \gg 1$): In this regime, the force-range is much larger than the length scale of the perturbation and eq. (27) for $\tilde{\chi}$ reduces to a Poisson-like equation for χ : $\nabla^2 \chi \propto \delta$; which is similar to the equation for Φ_+ and the effect of the modification is that the force is $4/3$ times its value in the absence of MG. Often, this effect is encapsulated by defining a modified Newton’s constant $G_{eff} = \frac{4}{3}G$. In this regime, the system is indifferent to the presence or absence of the Chameleon mechanism.

(ii) The weak-field regime ($Q \ll 1$): Here, the force range is much smaller than the length scale of the perturbation. The naive expectation is that the new fifth-force is unimportant and the dynamics will reduce to GR. However, χ is non-zero in this regime, the solution for χ can be approximated as $H^2 a^2 \Omega_m \tilde{x}_C^2 \delta$ and the extra force $\nabla \chi$ is proportional to $\nabla \delta$. We expect to see effects of the modification only in regions where the density changes over a length scale much smaller than the Compton wavelength. It is possible to obtain density enhancement at the top-hat edge even in the absence of the Chameleon screening as was demonstrated in NC22.

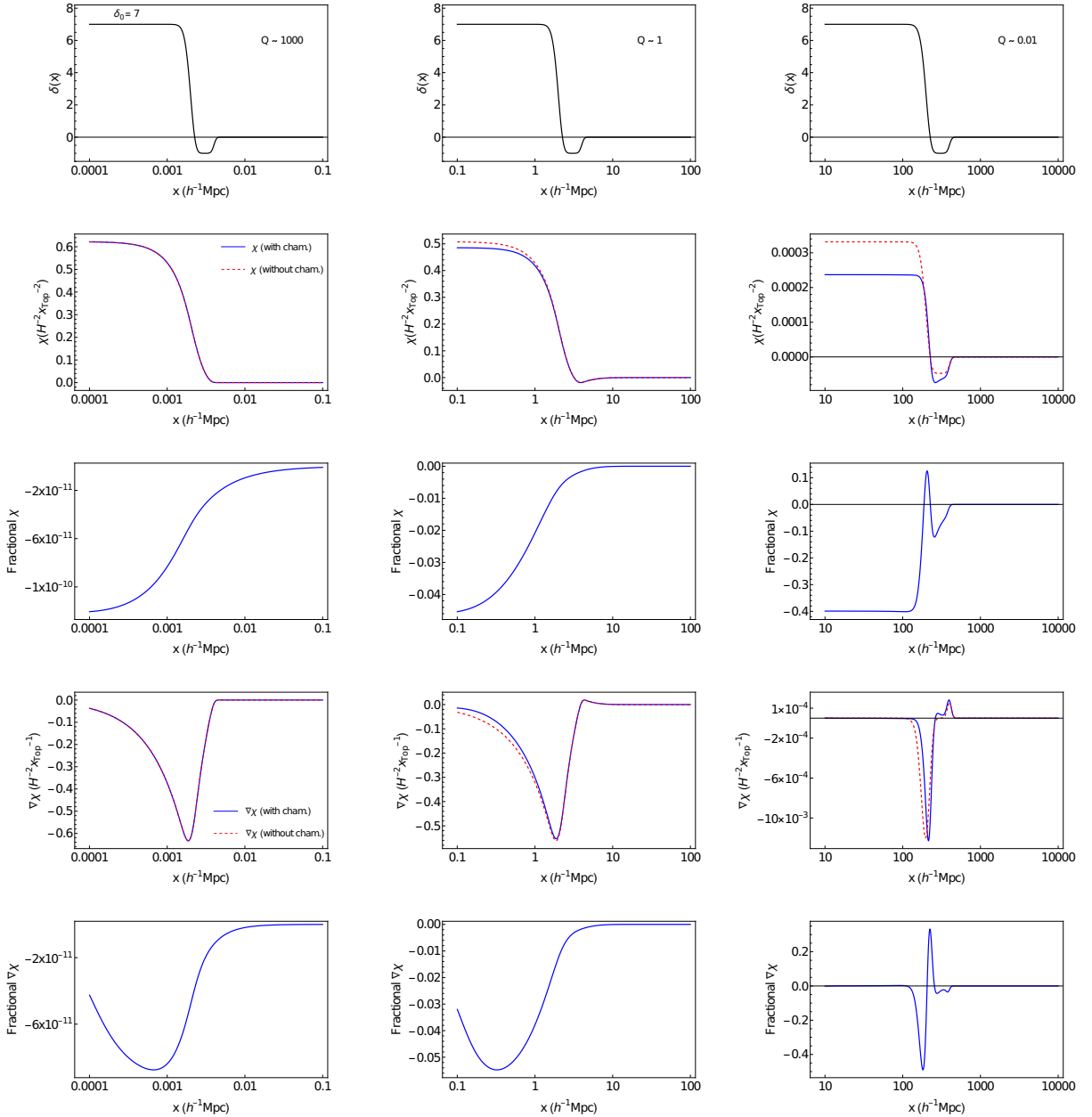


Figure 1. The spatial solutions for the dimensionless field χ , its gradient $\nabla\chi$ accounting for the chameleon mechanism. Fractional χ is the difference between χ and $\chi^{(1)}$ divided by the maximum value of χ . Here χ is the solution with the effects of the screening, and $\chi^{(1)}$ is the solution without the chameleon screening. Similarly, fractional $\nabla\chi$ is the difference between $\nabla\chi$ and $\nabla\chi^{(1)}$ divided by the minimum value of $\nabla\chi$.

(iii) The intermediate regime ($Q \sim 1$): In this regime, both terms in eq. (27) are important and the effect of the Chameleon screening can be seen in the dynamics of the perturbations.

5 RESULTS

We consider smoothed, compensated top-hat profiles with three different scales $x_{top} = 0.002, 2, 200, h^{-1}, \text{Mpc}$ (details in appendix). We classify them as strong, intermediate and weak field based on their values at $a = 1$ and refer to them as profile A, B and C respectively⁶. In figure 1 we consider a lower smoothing whereas in the remaining plots, we choose a

⁶ The strong and weak field profiles stay strong and weak throughout the evolution, whereas the intermediate field case can be considered to be in the weak field at early epochs

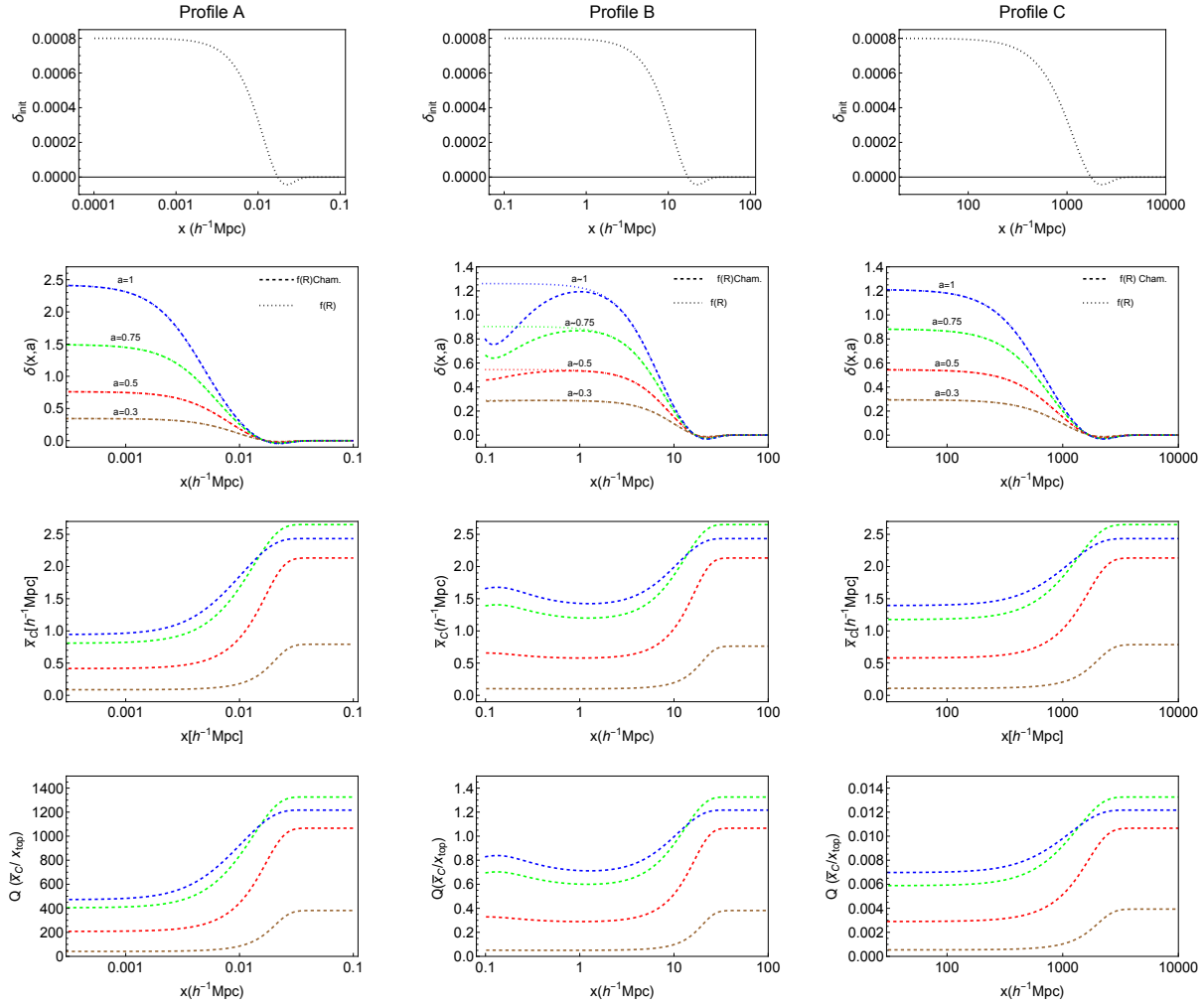


Figure 2. The Chameleon mechanism: spatio-temporal evolution of the density field and associated Compton scale. The initial profile (first panel), the evolved density (second panel), the scaled Compton wavelength (third panel) and the Q factor (fourth panel) plotted for three different initial profiles. Profile A stays in the strong field regime. The Chameleon mechanism does not manifest in this regime. Profile C stays in the weak field limit and again does not exhibit the Chameleon screening. Only profile B shows a change in behaviour due to the Chameleon screening.

higher smoothing parameter (details in the Appendix). The three profiles in each sector were evolved from $a = 0.001$ to $a = 1$ following the algorithm given in 4. At the end of each step, the Ricci scalar was computed using eq. (29) and the comoving Compton wavelength \bar{x}_C was computed using eq. (13) and (7). For this system, we examine the spatio-temporal evolution of the Compton scale in figure 2 and discuss the joint density-velocity evolution in figure 3 below.

5.1 Static solutions for χ using the iterative method

Figure 1 shows the solution for χ (scaled by $(Hx_{\text{top}})^2$ to make it dimensionless) with and without including Chameleon screening at $a = 1$ (fixed epoch). The solution with Chameleon is constructed by the series expansion (eq. (32)), kept upto the fourth order in ϵ as explained above. The solution without Chameleon corresponds to the first term of the series: $\chi^{(1)}$. The top panel shows the initial density profile. The lower four panels show the scaled χ and $\nabla\chi$ and the differences in the solutions with and without screening. As expected, in the strong field regime ($Q \gg 1$), including the Chameleon screening makes no difference to the solution for χ . In the weak field limit, the dimensionless χ is suppressed by the factor of $Q^2 \propto \bar{x}_C^2$. Since \bar{x}_C is lower in the presence of the Chameleon screening, the solution for χ is lower in magnitude as compared to the no Chameleon case.

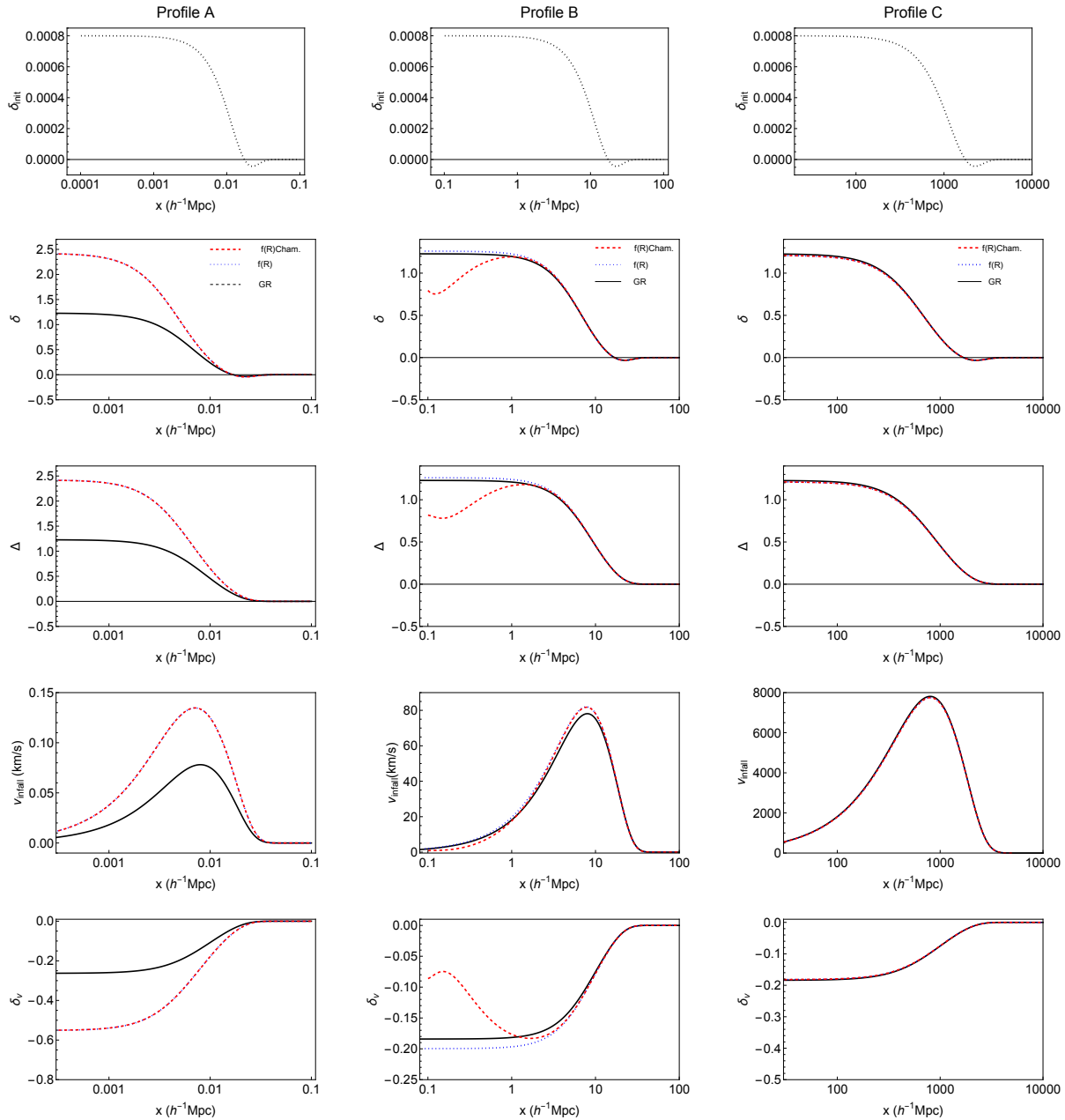


Figure 3. Non-linear evolution of density and velocity upto $a = 1$. The top panel plots the initial profiles at $a = 0.001$. The second, third and fourth panels show the density contrast δ , the spherically averaged density Δ and the infall velocity v_{infall} respectively at $a = 1$. The last panel shows the fractional Hubble parameter for each shell δ_v , which is a measure of the velocity divergence at that point. For profile A, there is an enhanced growth as compared to GR, but no effect of the Chameleon mechanism on the evolution. For profile C, the length scale is much larger than the Compton scale and the results are in agreement with GR. In this regime, the extra force is sensitive to the gradient of the density. For a smoothly varying profile, the density variation is also on scales larger than the Compton scale, resulting in agreement with GR. For profile B, the Chameleon mechanism suppress growth significantly both compared to GR and compared to the case when Chameleon is not invoked.

5.2 Spatio-temporal evolution of the Compton Scale

Figure 2 shows the evolution of the density field (second panel), the associated comoving Compton scale \bar{x}_C (third panel) as a function of the radial coordinate x for four different epochs $a \sim 0.3, 0.5, 0.75, 1$. The top panel shows the three initial profiles and the bottom panel shows the evolution of the parameter Q (defined in eq. (53)). In presence of perturbations, the Compton scale evolves both with time and space. We note that the background value of the Compton scale increases with epoch, only to show a slight decrease near the epoch of dark energy dominance.

Consider profile A. This profile is in the strong field regime throughout its evolution (as indicated by the value of Q). The Chameleon mechanism does not affect such a profile and the density evolution is the same with or without Chameleon.

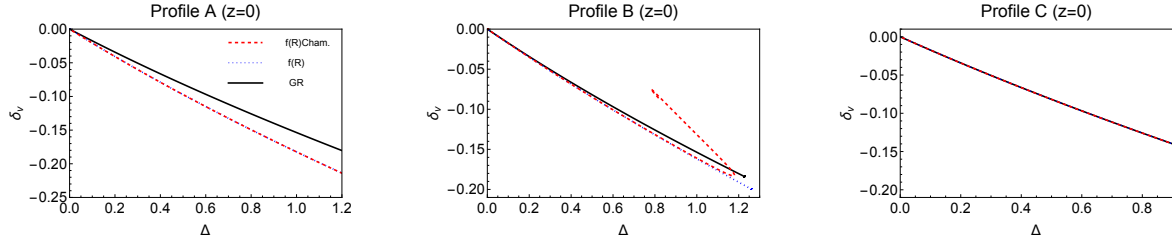


Figure 4. Evolution in the $\delta - \delta_v$ phasespace. As was seen in NC22, the evolution for profile A and profile C there is a unique density-velocity divergence relation at late times. However, for scales where the Chameleon mechanism is active, even for a single profile, the $\delta - \delta_v$ curve does not stay monotonic, but becomes a multi-valued function.

The Compton scale \bar{x}_C does evolve with density; it is lower in the high density regions but this evolution does not have a back-reaction on the density field. The potential is $4/3$ of its GR value and as we shall see in figure 3, the density grows faster than that in GR, as expected. Consider profile C. The Compton scale is much smaller than the scale of the perturbation and this profile stays in the weak field regime throughout its evolution. The effect of the modification is suppressed by a factor of Q^2 with or without Chameleon and the evolution is very close to that in GR (see figure 3). In this regime, the potential $\chi \propto \delta$ and the effect of the modification will be experienced only where δ changes on a scale smaller than the Compton wavelength. This can be understood from figure 1 and was also demonstrated in NC22 (fig. 12). Profile B has the most interesting evolution and is also the most astrophysically relevant situation. At early epochs $Q \ll 1$ and the profile can be considered in the strong field regime. The back-reaction of the spatially varying Compton scale does not affect the evolution and the shape of the perturbation is retained between until $a \sim 0.3$. The evolution is also linear since δ is small. As evolution proceeds, Q increases and the effect of the Chameleon mechanism starts to influence the evolution. At $a \sim 0.3$, \bar{x}_C is lower inside the perturbation as compared to outside. A lower value of \bar{x}_C in the inner shells means lower acceleration as compared to the outershells. Outer shells, as they approach the origin, encounter the relatively slower inner shells. This causes a mass build-up which is seen as a slight bump in the density field at $a \sim 0.5$. Consequently, the Chameleon scale also picks up a gradient in the inner regions: a relatively lower δ near the origin, implies a slight increase in \bar{x}_C near the origin at $a \sim 0.5$. This in turn affects further evolution of the density. Due to the increased value of \bar{x}_C near the origin, the shells that are falling inward near the origin experience higher force and accelerate faster towards the origin followed by slightly slower shells causing a second density enhancement near the origin at $a \sim 0.75$. This trend continues upto $a \sim 1$. We evolved this profile beyond $a > 1$ (not shown here) and found that the height of the increases with increase in final epoch. The enhancement near the origin did not propagate outwards and the final profiles looked qualitatively similar to the one shown here. The density enhancement at the edge of the top-hat is a known feature of the Chameleon mechanism and has been observed in earlier investigations Borisov et al. (2012); Kopp et al. (2013). However, the effect of that enhancement in the interior of the perturbation has not been captured by them and to the best of our knowledge has not been reported in the literature so far.

Figure 3 shows the density and velocity profiles at $a = 1$ for the same three initial conditions for three cases (i) $f(R)$ with Chameleon, (ii) $f(R)$ without Chameleon and (iii) standard GR Λ CDM. The overdensity (δ) and the spherically averaged overdensity (Δ) are in the second and third panels respectively. As expected, for profile A, the density grows faster than that in GR, whereas for profile C, it is indistinguishable from the GR evolution since the Compton scale is very small compared to the scale of the perturbation. The evolution of profile B is discussed in the earlier section. It is useful to note that while the profile without the Chameleon predicts slightly higher growth than the GR evolution, the Chameleon mechanism suppresses growth everywhere compared to GR. The density enhancement at the edge of the top-hat is a known feature of the Chameleon mechanism and has been observed in earlier investigations Borisov et al. (2012); Kopp et al. (2013), however, a comparison with GR has not been presented in these papers. The fourth panel shows the infall velocity defined as the negative of the peculiar velocity

$$v_{infall}(q, a) = -v(q, a). \quad (54)$$

For a perfect top-hat, the expected infall velocity is usually linear in the inner shells; but for the smooth profiles considered the peculiar velocity is maximum near the edge of the top-hat and then decreases monotonically in all three cases. For profile B, the difference in the evolution is not well-captured by the infall velocity. Instead, it is instructive to compute the profiles of the fractional Hubble parameter of the shell defined as

$$\delta_v = \frac{1}{H} \frac{\dot{r}}{r} - 1 = \frac{1}{H} \frac{v(q, a)}{a x(q, a)} = \frac{A'}{A}. \quad (55)$$

For a constant density profile, this is related to the scaled velocity divergence as $\Theta = 3\delta_v$. The profile for δ_v shows a clear distinction between the evolution with and without the Chameleon mechanism.

In figure 4, we plot the (Δ, δ_v) pairs at $z = 0/a = 1$. In standard GR, in linear theory, the density-velocity divergence

relation (DVDR) is linear: $\Theta = -aHf(\Omega_m)\Delta$. There have been extensions of this relation in the non-linear regime, starting with the early investigations based on perturbation theory and spherical collapse (Bernardeau 1992; Bilicki & Chodorowski 2008). Nadkarni-Ghosh (2013) (N13, hereafter) investigated this relation using spherical collapse, but not relying on the exact solutions of spherical geometry, but instead by imposing the condition of ‘no perturbations at the bang time’ to obtain unique (δ, δ_v) values at any epoch. This relation traces out a curve in the two-dimensional $\delta - \delta_v$ phasespace, which further turns out to be an invariant of the underlying dynamical system. The fact that is an invariant means that no matter what the initial conditions may be, the late-time non-linear density and velocity perturbations will always satisfy this relation. The fitting form provided in N13 also found to hold true for early dark energy models with a varying equation of state. More recently, in NC22, this dynamics was investigated for $f(R)$ models without the Chameleon field. In the strong field regime, where the equation has the same structure as GR a unique DVDR relation exists. In the weak field regime, the corrections to the dynamics are negligible and GR is reproduced. But, in general, in the intermediate regimes, the structure of the equations is such that the relation is dependent upon the shape of the initial profile, violating the invariant property seen in standard gravity. However, the relation always remains one-to-one. In the presence of the Chameleon mechanism, for profile B, the relation is no longer one-to-one even for a single profile. A given Δ value can have multiple δ_v values depending upon the location in the perturbation. This is fundamentally related to the non-linear feedback in built in the Chameleon mechanism. The density decides the value of the Compton scale, which in turn influences the density evolution. This behavior is different from the scatter in the DVDR relation observed in standard gravity in triaxial systems, where the multi-valued behaviour originates because of the three-dimensional nature of the dynamics.

6 DISCUSSION AND CONCLUSION

In this paper, we investigate the effect of the Chameleon mechanism on a smooth, compensated, top-hat density profiles evolving in a Universe with $f(R)$ gravity. In particular, we focus on the Hu-Sawicki model with parameters which are compatible with solar system constraints. This work builds on earlier investigation by one of the authors which considered the same system but ignored the Chameleon effect. The new addition to the earlier investigation is an iterative scheme for the scalar field potential $\chi = \Phi - \Psi$, which satisfies a non-linear differential equation. This has been solved in the past but with sophisticated two-point boundary value ODE solvers. The advantage of our method is that, although approximate, it is computationally inexpensive since each iteration uses an analytic solution to the linear differential operator which was developed in NC22.

We demonstrated the scheme on spherically symmetric top-hat profiles and reproduced the result which suggests a density-enhancement near the edge of the top-hat. Alongside, we also explicitly solve for the spatio-temporal evolution of the Compton scale. We also found that the Chameleon screening can suppress growth compared to standard gravity even when ignoring screening predicted an enhancement. The main advantage of this scheme is that it enables a straightforward generalization to generic 3D initial conditions because each iteration can be solved using Fourier transforms and can be coupled to a Lagrangian Perturbative Scheme (Nadkarni-Ghosh & Chernoff 2011, 2013) fairly easily. We leave this for future investigation.

7 ACKNOWLEDGEMENTS

S. N-G would like to thank IIT Kanpur for the Initiation Grant (SSA/2022232) and the Department of Science and Technology, ANRF (previously Science and Engineering Research Board) for the MATRICES grant (No.MTR/2023/001376). T.R.V. would like to thank the SURGE programme at IIT Kanpur, which enabled the start of this project. Data generated by the numerical runs available on request from the corresponding author.

References

Alam S. et al., 2017, *Monthly Notices of the Royal Astronomical Society*, 470, 2617

Alam S. et al., 2020, arXiv e-prints, 2011, arXiv:2011.05771

Amendola L. et al., 2018, *Living Reviews in Relativity*, 21, 2

Aviles A., Cervantes-Cota J. L., 2017, *Physical Review D*, 96

Bardeen J. M., Bond J. R., Kaiser N., Szalay A. S., 1986, *The Astrophysical Journal*, 304, 15

Bean R., Bernat D., Pogosian L., Silvestri A., Trodden M., 2007, *Physical Review D*, 75, 064020

Bernardeau F., 1992, *The Astrophysical Journal*, 390, L61

Bernardeau F., Chodorowski M. J., Lokas E. L., Stompor R., Kudlicki A., 1999, *Monthly Notices of the Royal Astronomical Society*, 309, 543

Bilicki M., Chodorowski M. J., 2008, *Monthly Notices of the Royal Astronomical Society*, 391, 1796

Borisov A., Jain B., Zhang P., 2012, *Physical Review D*, 85, 63518

Bose B. et al., 2024, arXiv

Brax P., Rosenfeld R., Steer D., 2010, *Journal of Cosmology and Astroparticle Physics*, 2010, 033–033

Brax P., van de Bruck C., Davis A., Green A., 2006, *Physics Letters B*, 633, 441–446

Cataneo M., Uhlemann C., Arnold C., Gough A., Li B., Heymans C., 2021, The matter density pdf for modified gravity and dark energy with large deviations theory

Chodorowski M. J., Lokas E. L., 1997, *Monthly Notices of the Royal Astronomical Society*, 287, 591

Chodorowski M. J., Lokas E. L., Pollo A., Nusser A., 1998, *Monthly Notices of the Royal Astronomical Society*, 300, 1027

Clifton T., Ferreira P. G., Padilla A., Skordis C., 2012, *Physics Reports*, 513, 1

De Felice A., Tsujikawa S., 2010, *Living Reviews in Relativity*, 13, 3

Herrera D., Waga I., Jorâjs S. E., 2017, ArXiv e-prints, 1703, arXiv:1703.05824

Hu W., Sawicki I., 2007, *Physical Review D*, 76, 104043

Joyce A., Jain B., Khoury J., Trodden M., 2015, *Physics Reports*, 568, 1

Joyce A., Lombriser L., Schmidt F., 2016, *Annual Review of Nuclear and Particle Science*, 66, 95

Khoury J., Weltman A., 2004a, *Physical Review D*, 69, 044026

Khoury J., Weltman A., 2004b, *Physical Review Letters*, 93

Kopp M., Appleby S. A., Achitouv I., Weller J., 2013, *Physical Review D*, 88, 084015

Koyama K., Taruya A., Hiramatsu T., 2009, *Physical Review D*, 79

Lam T. Y., Li B., 2012, *Monthly Notices of the Royal Astronomical Society*, 426, 3260–3270

Lee J., Jing Y. P., Suto Y., 2005, *The Astrophysical Journal*, 632, 706–712

Li B., Efstathiou G., 2012, *Monthly Notices of the Royal Astronomical Society*, 421, 1431

Li B., Lam T. Y., 2012, *Monthly Notices of the Royal Astronomical Society*, 425, 730–739

Llinares C., 2018, *International Journal of Modern Physics D*, 27, 1848003

Lombriser L., 2016, *Journal of Cosmology and Astro-Particle Physics*, 11, 039

Lombriser L., Li B., Koyama K., Zhao G.-B., 2013, *Physical Review D*, 87

Lopes R. C., Voivodic R., Abramo L. R., Jr. L. S., 2018a, *Journal of Cosmology and Astroparticle Physics*, 2018, 010–010

Lopes R. C. C., Voivodic R., Abramo L. R., Sodrâo Jr L., 2018b, arXiv:1805.09918 [astro-ph], arXiv: 1805.09918

Mandal A., Nadkarni-Ghosh S., 2020, *Monthly Notices of the Royal Astronomical Society*, 498, 355

Nadkarni-Ghosh S., 2013, *Monthly Notices of the Royal Astronomical Society*, 428, 1166

Nadkarni-Ghosh S., Arya B., 2018, *Monthly Notices of the Royal Astronomical Society*, 475, 3553

Nadkarni-Ghosh S., Chernoff D. F., 2011, *Monthly Notices of the Royal Astronomical Society*, 410, 1454

Nadkarni-Ghosh S., Chernoff D. F., 2013, *Monthly Notices of the Royal Astronomical Society*, 431, 799

Nadkarni-Ghosh S., Chowdhury S., 2022, *Monthly Notices of the Royal Astronomical Society*, 511, 3636–3656

Nadkarni-Ghosh S., Singhal A., 2016, *Monthly Notices of the Royal Astronomical Society*, 457, 2773

Nojiri S., Odintsov S., Oikonomou V., 2017, *Physics Reports*, 692, 1–104

Oyaizu H., 2008, *Physical Review D*, 78, 123523

Oyaizu H., Lima M., Hu W., 2008, *Physical Review D*, 78, 123524

Pogosian L., Silvestri A., 2008, *Physical Review D*, 77, 023503

Press W. H., Schechter P., 1974, *Astrophysical Journal*, 187, 425

Puchwein E., Baldi M., Springel V., 2013, *Monthly Notices of the Royal Astronomical Society*, 436, 348–360

Schmidt F., Lima M., Oyaizu H., Hu W., 2009, *Physical Review D*, 79, 83518

Sheth R. K., Mo H. J., Tormen G., 2001, *Monthly Notices of the Royal Astronomical Society*, 323, 1–12

Song Y.-S., Hu W., Sawicki I., 2007, *Physical Review D*, 75, 044004

Sotiriou T. P., Faraoni V., 2010, *Reviews of Modern Physics*, 82, 451

Tassev S., Zaldarriaga M., Eisenstein D. J., 2013, *Journal of Cosmology and Astroparticle Physics*, 2013, 036–036

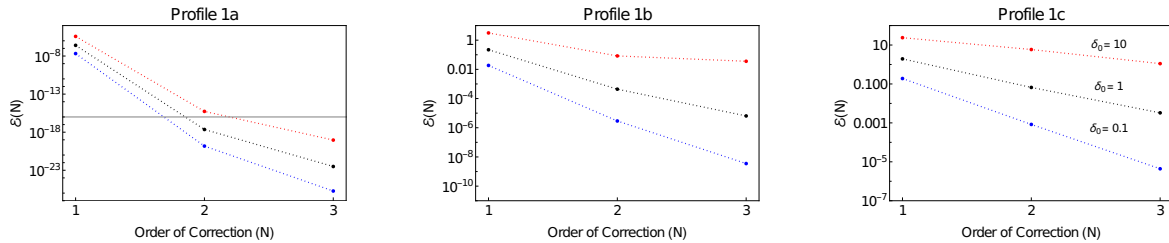


Figure A1. Convergence test of the Taylor expansion. Comparison of successive terms in the Taylor expansion of χ at $a=1$ using 500 spatial points. $\mathcal{E}(N)$ has been calculated up to $\delta_0 = 30$ and we observe convergence up to $\delta_0 = 15$.

Tsujikawa S., 2013, Classical and Quantum Gravity, 30, 214003
 Tsujikawa S., Amendola L., 2015, Dark Energy: Theory and Observations. Cambridge University Press
 Valogiannis G., Bean R., 2017, Physical Review D, 95
 Vraštil M., Habib S., 2020, Monthly Notices of the Royal Astronomical Society, 493, 2085
 Wetterich C., 2015, Lecture Notes in Physics, Berlin Springer Verlag
 Winther H. A., Koyama K., Manera M., Wright B. S., Zhao G.-B., 2017, Journal of Cosmology and Astroparticle Physics, 2017, 006–006
 Winther H. A. et al., 2015, Monthly Notices of the Royal Astronomical Society, 454, 4208
 Zhao G.-B., Li B., Koyama K., 2011, Physical Review D, 83
 Zheng Z., Schneider M., Amendola L., 2025, arXiv e-prints, arXiv:2511.11554

APPENDIX A: CONVERGENCE TESTS.

A1 Convergence of the iterative solution for χ .

The initial profiles used are identical to the top-hats used in NC22. The profile parameters and the initial profiles used for each figure are listed in the tables below.

The error is defined as :

$$\mathcal{E}(N) = \text{Max}\{\chi_N - \chi_{N-1}\} \quad (\text{A1})$$

where "N" is the order of the Taylor expansion and $\chi(N)$ is the solution to χ corresponding to the N^{th} order.

A2 Convergence of the Algorithm for the temporal evolution - solution of χ

The error is defined as :

$$\mathcal{E}(N) = \text{Max}\{\chi_{(n2_t \times n2_s)} - \chi_{n1_t \times n1_s}\} \quad (\text{A2})$$

where "N" is the order of the Taylor expansion and $\chi(N)$ is the solution to χ corresponding to the N^{th} order.

APPENDIX B: NUMERICAL RUNS

Numerical instability for profile C: We plotted χ and observed that for small values of Q , corresponding to small χ ($\approx 10^{-7}$), the outermost shells are not resolved when using the integration method to compute χ . Hence, why we switched to using an approximation for profile C, up to $Q = 0.027$ based on the proportionality relation between χ and δ in this regime.

Numerical instability due to the approximation: Switching to the approximation and taking manual derivatives of the approximate solution for χ , leaves us subject to the Courant–Friedrichs–Lowy condition,

$$\frac{u\Delta t}{\Delta x} = C \leq C_{\text{max}} \quad (\text{B1})$$

where Δt is temporal grid resolution, Δx is the spatial grid resolution. C_{max} is a dimensionless quantity that depends on the approximation scheme. For values of C that violate this condition, we expect the scheme to numerically collapse. A straightforward fix would be to take a finer temporal grid, but this leads to the inner shells of the profiles not being resolved in our scheme. To resolve these inner shells, we require a finer spatial grid. This leads to an interesting trade-off in choosing the grid resolution. Choosing the temporal grid too fine leads to us losing the inner shells, where choosing a finer spatial grid could cause the scheme to collapse. With this trade-off in mind, the grid sizes are chosen in all our runs.

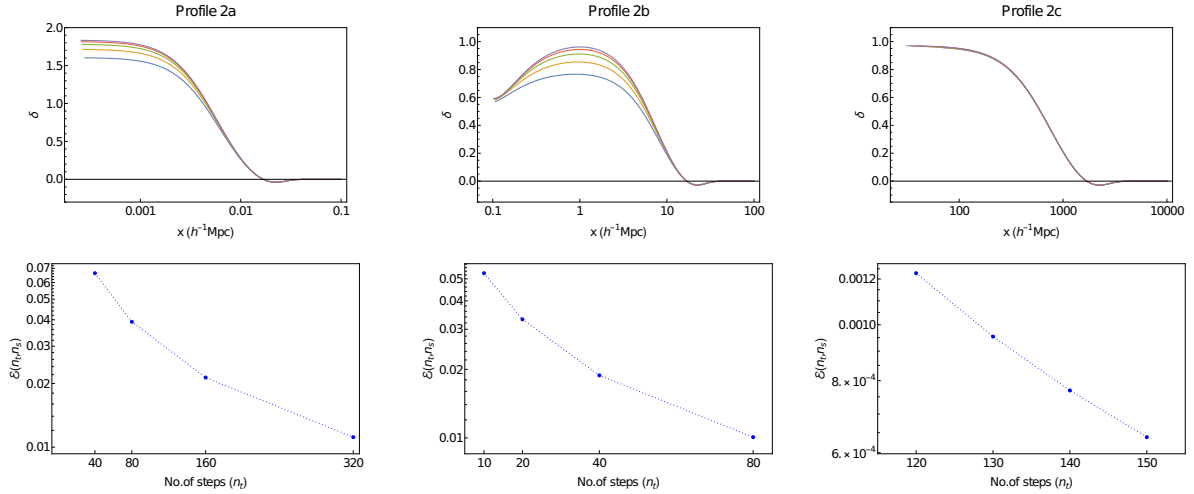


Figure A2. Convergence test of the full algorithm. $\mathcal{E}(N)$ is plotted against n_t . The grid sizes corresponding to the profiles are provided in Table B3.

Profile Name	σ	x_{top}	Q (for $f_{R0} = -10^{-6}$)	$L_{\min} (h^{-1} \text{Mpc})$	$L_{\max} (h^{-1} \text{Mpc})$
1a	0.0025	0.002	1217	0.0001	0.1
1b	0.0025	2	1.21	0.1	100
1c	0.0025	200	0.012	10	10000
2a	0.1	0.002	1217	0.0001	0.1
2b	0.1	2	1.21	0.1	100
2c	0.1	200	0.012	10	10000

Table B1. Table denoting the parameters of the two profiles used.

Figure	Profile used	A	N_s	N_t	a_{switch}	a_{final}
figure 1	1a,b,c	7	3000	—	—	—
figure 2, 3, 4	2a,b,c	0.0008	1600,3200,700	320,80,150	0.1	1

Table B2. Table listing, for each figure, the profiles and numerical parameters used.

Profile used	A	N_s	N_t	a_{switch}	a_{final}
2a	0.0008	{100, 200, 400, 800, 1600}	{20, 40, 80, 160, 320}	0.1	1
2b	0.0008	{200, 400, 800, 1600, 3200}	{5, 10, 20, 40, 80}	0.1	1
2c	0.0008	{300, 400, 500, 600, 700}	{110, 120, 130, 140, 150}	0.1	1

Table B3. Table listing, for each figure, the profiles and numerical parameters used.